# *Atomic-resolution electron microscopy of nanoscale local structure in lead-based relaxor ferroelectrics*

# Atomic-resolution electron microscopy of nanoscale local structure in lead-based relaxor ferroelectrics

Abinash Kumar[1], Jonathon N. Baker[2], Preston C. Bowes[2], Matthew J. Cabral[2], Shujun Zhang[3], Elizabeth C. Dickey[2], Douglas L. Irving[2], James M. LeBeau[1]

[1]Department of Materials Science and Engineering, Massachusetts Institute of Technology, Cambridge, MA 02139, USA
[2]Department of Materials Science and Engineering, North Carolina State University, Raleigh, North Carolina 27695, USA
[3]Institute for Superconducting and Electronic Materials, Australian Institute of Innovative Materials, University of Wollongong, Wollongong, NSW 2500, Australia

**Abstract**

Relaxor ferroelectrics, which can exhibit exceptional electromechanical coupling, are some of the most important functional materials with applications ranging from ultrasound imaging to actuators. Since their discovery, their complexity of nanoscale chemical and structural heterogeneity has made understanding the origins of their electromechanical properties a seemingly intractable problem. Here, we employ aberration-corrected scanning transmission electron microscopy (STEM) to quantify various types of nanoscale heterogeneities and their connection to local polarization in the prototypical relaxor ferroelectric system $Pb(Mg_{1/3}Nb_{2/3})O_3$-$PbTiO_3$ (PMN-PT). We identify three main contributions that each depend on Ti content: chemical order, oxygen octahedral tilt, and oxygen octahedral distortion. These heterogeneities are found to be spatially correlated with low angle polar domain walls, indicating their role in disrupting long-range polarization and leading to nanoscale domain formation and the relaxor response. We further locate nanoscale regions of monoclinic- like distortion that correlate directly with Ti content and electromechanical performance. Through this approach, the connection between chemical heterogeneity, structural heterogeneity and local polariza-

tion is revealed, validating models that are needed to develop the next generation of relaxor ferroelectrics.

Relaxor ferroelectrics are distinguished from traditional ferroelectrics by their frequency dependent, diffuse phase transitions that are commonly attributed to the existence of nanoscale order.[1] Among this class of materials, Pb-based systems remain essential as they exhibit the largest known piezoelectric coefficients and outstanding dielectric properties.[2–4] These properties have been commonly attributed to the existence of polar nanoregions in the material that align to the applied field.[5,6] This simple model fails, however, to explain relaxor behavior in a variety of materials, including polymer-based systems.[7] The recently proposed "polar slush" model overcomes these limitations by considering a multi-domain polar state with low energy, low angle domain walls formed throughout.[8] Model validation has, however, been hindered by the seemingly endless number of structural characterization studies with differing interpretations, leading these systems to be described as a "hopeless mess".[1]

$Pb(Mg_{1/3}Nb_{2/3})O_3$-$PbTiO_3$ (PMN-PT) is the prototypical Pb-based relaxor ferroelectric system and exhibits state-of-the-art properties. For example, piezoelectric constants up to 4100 pC/N have been achieved via Sm doping[9]. PMN-PT adopts the perovskite structure (formula $ABO_3$) with the A sub-lattice occupied by Pb and the B sub-lattice occupied by the either Mg, Nb, or Ti. Furthermore, as $PbTiO_3$ is added to PMN, the system reaches a morphotropic phase boundary (MPB) near PMN-30PT where the electromechanical properties are maximized.[10] Deciphering the origins of these enhanced properties is, however, complicated by nanoscale heterogenity of chemistry and structure. While X-ray and neutron scattering are the predominate characterization methods used to explain these details, making direct connections between composition, structure, and polarization have proven exceedingly difficult[11–17]. For example, while nanoscale chemical ordering of the B sub-lattice cations was one of the first signatures revealed[17,18] and is found to varying degrees in all Pb-based relaxor ferroelectrics[19,20], its details are still being explored[21–23].

Capturing a complete picture of the connection between chemistry, structure, and polariza-

tion in relaxor ferroelectrics requires characterization techniques that are able to account for both cation *and* anion sub-lattices. While distortions of the oxygen sub-lattice have been previously detected[24], a combination of X-ray and neutron diffraction recently discovered that correlated oxygen displacements are likely integral to bringing forth the outstanding electromechanical properties in PMN-PT[10]. Diffraction characterization methods, however, lack the spatial resolution required to directly determine the origin of nanoscale polar variation[25,26]. In contrast, annular dark-field scanning transmission electron microscopy (ADF STEM), Figure 1a, can readily image the projected crystal structure at the atomic length scale and is sensitive to chemical distribution[21]. Unfortunately, ADF images are dominated by cation contrast that precludes detailed detection and quantification of light elements such as oxygen. Recently, annular bright field (ABF)[27,28] and integrated differential phase contrast (iDPC)[29,30] STEM techniques have been developed to overcome these challenges. While iDPC can detect the cation and oxygen atom column positions, as shown in Figure 1a, it too has a major drawback: the image contrast lacks the atomic number interpretability of ADF STEM. On the other hand, both limitations can be overcome by simultaneously capturing ADF and iDPC images, with the resulting datasets akin to merging results from X-ray and neutron diffraction techniques, and enabling correlation between polarization, chemistry, and structure directly at the atomic scale.

Here, we investigate the structural and chemical origins of relaxor ferroelectric properties in PMN-xPT (x=0, 10, and 30). Through a combination of ADF and iDPC aberration corrected STEM, the projected positions of cation and anion sub-lattices are used to measure the subtle features of nanoscale polarization in these materials. The projected polarization reveals the presence of nanoscale domains that are consistent with the polar slush model.[8] We further quantify the distribution of chemical and structural heterogeneities as a function of Ti content, and a direct correlation is found between the spatial distribution of chemical/structural heterogeneities and polarization domain walls. The heterogeneities are found to inhibit polarization rotation, leading to the formation of low angle domain walls. In combination, these results provide evidence for the

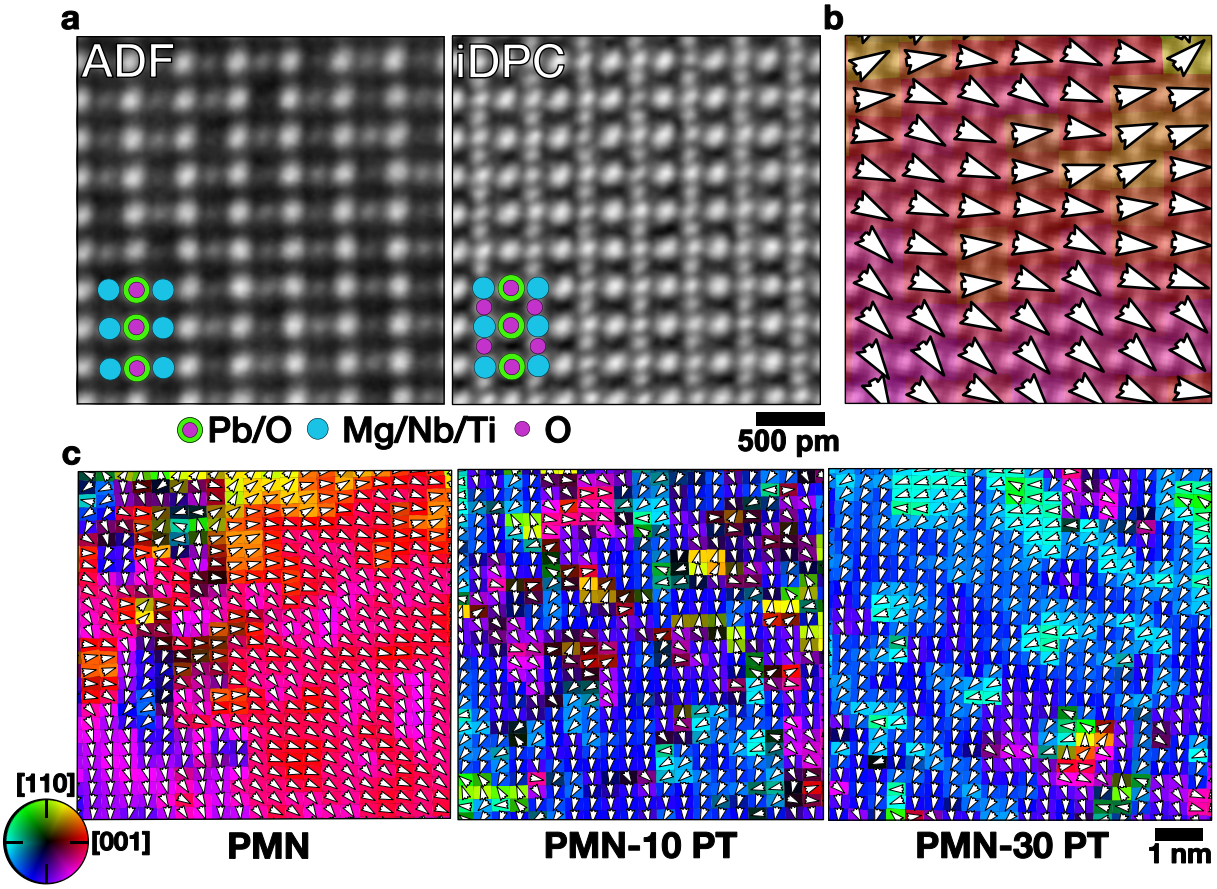


Figure 1: (a) Simultaneously acquired ADF and iDPC images of PMN along the $\langle 1\bar{1}0 \rangle$ projection with the (b) projected displacement (polarization) map from iDPC. (c) Projected displacement (polarization) for PMN-xPT (x=0, 10, and 30) unit cells in representative iDPC images. The projected displacement(polarization) magnitude ranges from 1 to 20 pm, and is indicated by luminosity.

underlying mechanisms responsible for yielding relaxor behavior.

## Mapping nanoscale polarization variation

Using iDPC STEM, the projected polarization is measured across ten different sample locations using the approach outlined in the Methods, and the influence of projection on these measurements is explored in Supplementary Information Section S1. These datasets yields approximately 5,000 analyzed unit cells at each of the three PMN-PT compositions. The high sampling of each composition provides a statistical representation of the underlying structure of the material, aid-

ing in connecting the results presented here to prior diffraction studies. Calculating the center of mass difference between the cations and anions using iDPC STEM, Figure 1c shows representative projected polarization maps for PMN, PMN-10PT, and PMN-30PT imaged along $\langle 1\bar{1}0 \rangle$. The projected polarization exhibits regions with similar magnitude and direction, i.e. polar domains, that vary smoothly across each image.

Notably for PMN, the observed polar domains do not decay to a non-polar background, which contrasts with the polar nanoregion model that assumes a non-polar matrix. These nanoscale domains vary in size from 2-12 nm and form low angle domain walls between them, which are located using the method described in Supplementary Information Section S2. This observation is also remarkably similar to reverse Monte Carlo analysis of diffraction data.[23] Moreover, a significant majority (72%) of the domain wall angles are in the range of 10-35° , which is in agreement with predictions from the polar slush model (see Supplementary Information Section S2).[8,31] As the fraction of PT increases, the average domain wall angle increases, reflecting the onset of ferroelectric behavior. This behavior leads to the mixed relaxor and ferroelectric properties found in PMN-PT materials and expected from the polar slush model.[8,31] This model does not, however, incorporate the specific structure and chemistry details that drive the formation of the polar domains.

## Quantifying the types of local order

Chemical ordering is revealed in the ADF STEM data, as shown in Figure 2a,left. Clustered oscillation of B sub-lattice atom column intensity on (111) planes indicates a doubled perovskite lattice where occupancy of Mg and Nb vary systematically. The weaker normalized intensity atom columns (blue) contain more Mg or Ti ($\beta_I$), while those stronger intensity atom columns (red) contain more Nb ($\beta_{II}$). Correlation analysis, shown in Figure 2a and detailed in Supplementary Information Section S3, is used to quantify the relative fraction of these chemically ordered regions (CORs). At each composition, the CORs are found throughout and account for 39$\pm$1% of

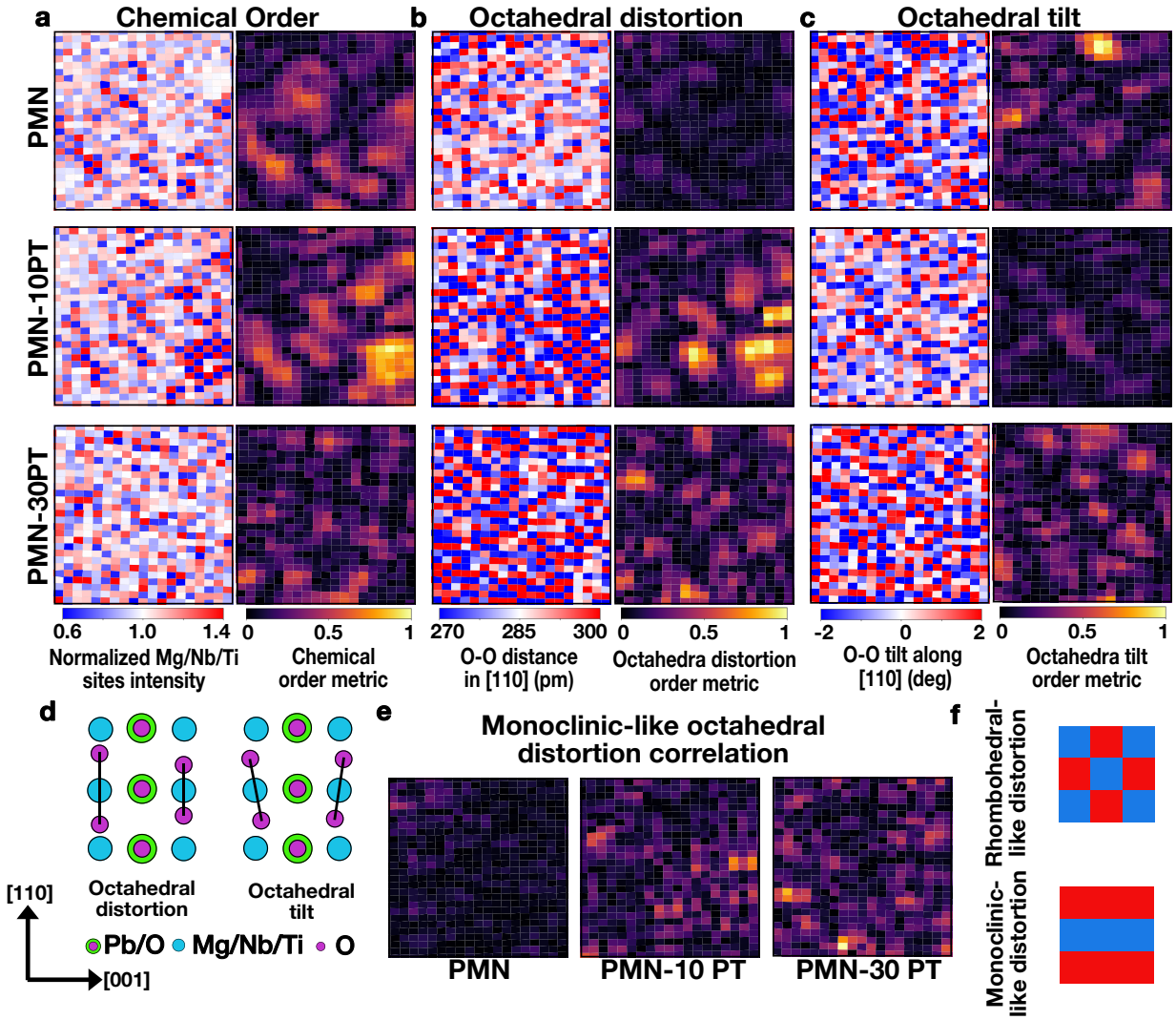


Figure 2: Spatial distribution of structural and chemical heterogeneities, (a) chemical order, (b) octahedral distortion, (c) octahedral tilt, (d) schematic of distortion types and their corresponding O-O patterns, (e) monoclinic-like distortion analysis, and (f) schematic patterns of rhombohedral-like and monoclinic-like distortion.

the total projected area in the case of PMN, 37±2% for 10% of PT, and only 11±1% for 30% PT. The decreasing chemical order with increasing Ti is in agreement with previous X-ray and neutron scattering results where superlattice reflection intensity also decreases as the composition approaches the MPB.[10,32]

Recently, Krogstad suggested the presence of anti-ferrodistortive displacements based on diffuse scattering features, i.e. Pb displaces in the opposite direction of its B sub-lattice neighbors[10]. The chemical and spatial origins of this behavior could not, however, be unambiguously determined. From iDPC STEM data, the Pb atom columns are anti-ferrodistortive relative to the B-sites largely in the CORs, (Supplementary Information Section S4). These anti-ferrodistortive displacements decrease in accordance with the decreasing COR density as PT content increases, and in agreement with Krogstad.

As noted from recent X-ray and neutron scattering experiments, oxygen displacements may hold the key to understanding structure-property relationships in Pb-based relaxors.[10] To this end, oxygen octahedral distortion (expansion/compression) and tilting (schematically shown in Figure 2d) are determined from iDPC images, as in Figures 2b-c. At each composition, distortion and tilting exhibit local ordering, reminiscent of the CORs.

Similar correlation analysis (see Supplementary Information Section S3) is used to determine the area fraction of octahedral distortion regions (ODRs), as shown in Figure 2b. In PMN, 21% of the projected area exhibits distortion ordering, with 63% overlapping the CORs and 27% at the COR boundaries.The overlap of the CORs and ODRs highlights the spatial correlation between octahedral distortion and chemical ordering. As PT content increases, the ODRs increase to 28% for PMN-10PT. Furthermore, a similar checkerboard octahedral distortion pattern is predicted for the chemically ordered PMN from density functional theory (DFT) (Supplementary Information Sections S5 and S6).

At PMN-30PT, however, the distortion order changes. Rather than exhibiting the rhombohedral-like, checkerboard distortion pattern (see Figure 2f), the distortion becomes predominately striped

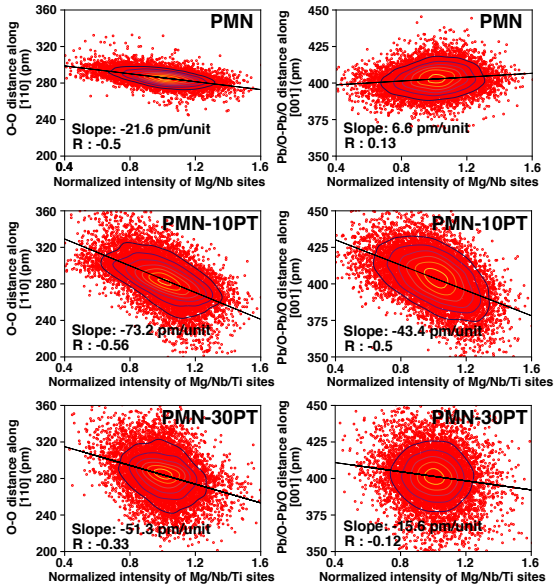


Figure 3: Correlation between the Mg/Nb/Ti normalized atom column intensity and the O-O distance along $[110]$ or Pb/O-Pb/O distance along $[001]$ as indicated.

on $(110)$ planes, which indicates the formation of monoclinic-like unit cells as verified with STEM image simulations (Supplementary Information Figure S11) and agrees with prior diffraction studies[11]. The area fractions of rhombohedral- and monoclinic-like distortions were determined by use of the correlation analysis approach discussed in Supplementary Information Section S3. As Ti content increases so too does monoclinic-like distortion as shown in Figure 2e. Moreover, this type of local planar distortion should give rise to asymmetric diffuse scattering[33]. Importantly, Krogstad[10] found that the oxygen-mediated asymmetric diffuse scattering in neutron scattering was the only feature linked to the piezoelectric properties. The results presented here confirm that oxygen displacements are key and they originate in monoclinic-like regions. It is also important to note that due to presence of gradients in local chemistry and structure, pure phases (rhombohedral or monoclinic) are not observed. From this, one can argue that such strong local structural variations and short correlation lengths give rise to local triclinic symmetry, which can facilitate the free rotation of polarization by small angles. This finding further supports the polar slush model's description of relaxors.

Beyond expansion and contraction, the oxygen octahedra also tilt with respect to $[110]$, as shown in Figure 2c. Applying correlation analysis (see Supplementary Information Section S3), 19% of the total projected area exhibits octahedral tilt ordering in PMN. Analysis of the B sublattice atom column intensities in and around these octahedral tilt regions (OTRs) shows that the atom column intensities are normally distributed (see Supplementary Information Section S7). Thus the OTRs do not occur at the interior of the CORs, but that they form in close proximity to the boundary between CORs. Furthermore, these regions are rich in magnesium, as exhibited by the shift in mean column intensities towards lower values (Supplementary Information Figure S13). Taken together with the DFT determined bond length distributions, these findings suggest a mechanism for the OTRs. Specifically, Mg-O bond lengths are much more strongly conserved than Nb-O bond lengths. As a result, Mg-O-Mg bonded octahedra would be more likely to tilt rather than stretch. Moreover, because Mg-O-Mg bonds can only exist in regions that are not chemically ordered (Supplementary Information Figure S7), such tilting is expected to be especially pronounced in transition regions due to the change in local chemistry.

The anti-phase tilt pattern suggest the presence of local rhombohedral, $R3c$ local symmetry.[34] With increasing PT, the OTR area decreases from 11% to 5% for 10PT and 30PT, respectively. As the fraction of these features decrease with composition, their disappearance also explains another distinct diffuse scattering contribution noted by Krogstad that had both temperature dependent and independent components. While the temperature independent contribution is thought to originate from the CORs, the temperature dependent part then arises from the octahedral tilt ordering that is disrupted by thermal fluctuations. The intensity of this type of diffuse scattering is found to decrease with PT content and follows the same trend as OTRs quantified from STEM.

## Relating local chemistry and structure

Combining the ADF and iDPC STEM data, the change in B site chemistry measured with the Mg/Nb/Ti atom column intensity is also found to correlate to the O-O neighbor distance, as shown

in Figure 3. In each case, the B sub-lattice intensity is negatively correlated with the O-O atom column distances[35].This shows that Mg/Ti expands the local oxygen sub-lattice, while Nb leads to contraction, which is consistent with the prior reports.[23,36,37]. In combination with the response of oxygen at the MPB where the O-O spread increases, the observed correlation indicates the key role of Ti to disrupt the lattice to stabilize the monoclinic-like distortion and increase the piezoelectric coefficient. The Pb/O-Pb/O atom column distances, in comparison, show weak-to-no correlation with variation in B-site chemistry in PMN as shown in Figure 3, likely due to the dominant contribution of Pb on the observed atom column positions (Supplementary Information Section S1).

PMN-10PT, in contrast, exhibits moderate, negative correlation as shown in Figure 3. At the MPB, PMN-30PT, significantly larger distortions are observed that correspond to the increased polarization and piezoelectric coefficient. This correlated structural variation in Pb displacement also explains the diffuse scattering feature found by Krogstad that correlates to the cation size mismatch. Furthermore, the above mentioned correlation is significant as nearly $\approx$10,000 atom columns are used in the analysis.

Further analysis of the PMN-10PT $\beta_I$ and $\beta_{II}$ normalized intensities (Supplementary Information Figure S12) also reveals that their intensity difference is enhanced with the introduction of Ti. This suggests that Ti initially replaces Nb in the mixed $\beta_I$ sites of the CORs leading to a concomitant decrease in intensity for those atom columns and increased image contrast. Importantly, the preferential incorporation of Ti to the CORs has not been previously shown and can be explained by analysis of the B sub-lattice bond lengths from DFT, albiet via an indirect argument. Any covalent bond has an ideal length or range of lengths it prefers to adopt for any particular coordination environment, and adopting bond lengths outside of this range is associated with severe energetic penalties and a commensurate decrease in the likelihood of incorporation. For example in oxide perovskites, titanium tends to prefer bond lengths between 1.9 and 2.2 Å[38–41]. Supplementary Figure S8 shows the ratio of B-sites in the simulated COR and disordered structures with bond lengths

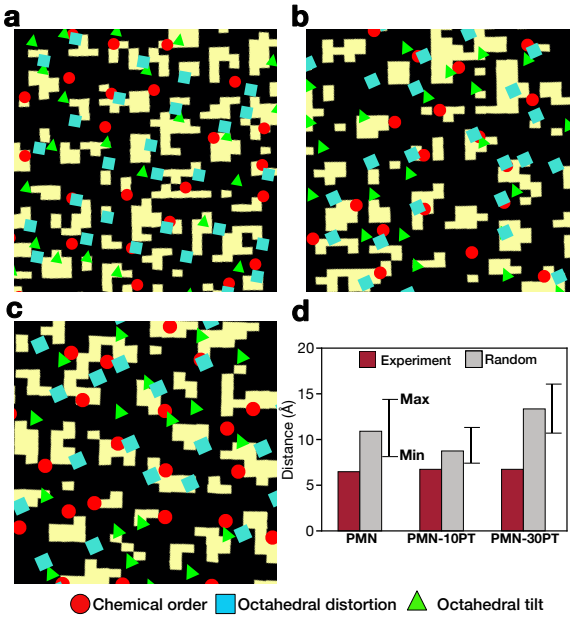


Figure 4: Positions of CORs, ODRs, OTRs, and domain walls for (a) PMN, (b) PMN-10PT, and (c) PMN-30PT. (d) Nearest distance between 95 % of heterogeneities maxima (random points) and domain wall for each PMN-xPT composition. Domain walls occur at the blocked, yellow regions.

within a certain range. It is clear from this figure that, for a given bond length window, the COR structure has significantly more sites close to Ti's ideal octahedral bonding environment than the disordered structure, especially when considering 5 and 6 B-O bonds. In fact, the COR structure has between 2 and 3 times more sites available than the disordered structure over most of the bond length range considered, and nearly 20 times more in the most extreme case. These high ratios result from the 2-4 pm differences in the onset of optimal coordination environments between the two systems, and indicate that Ti can form more strong bonds in the chemically ordered regions than in the disordered regions without changing any other bond lengths or otherwise altering the structures. All else being equal, this strongly suggests that Ti will preferentially incorporate into the CORs, at least on the PMN side of the composition space where CORs form.

## Linking polarization and heterogeneity

The heterogeneity distribution is also found to link directly with the local variation in polarization and domain walls. First, the centers of the CORs, ODRs, and OTRs are identified as maxima in the results from correlation analysis as detailed in Supplementary Information Section S8. Qualitatively, Figure 4a-c, the heterogeneity maxima occur at, or very near, the locations of greatest polarization variation, i.e. low angle domain walls.

The observed relationship between ordered heterogeneities and domains walls is validated by quantifying the nearest neighbor distance. As shown in Figure 4d, 95% of the heterogeneities are within a distance of 1.5-2 unit cells of the nearest domain wall regardless of PT content. Across the composition range investigated, 1/3 of CORs, 1/3 ODRs, and 1/3 OTRs are within this distance of the domain walls. In addition, 1/3 of the domain walls have at least two nearby types of structural or chemical ordering. This indicates that the polar domain walls cannot be explained by a single type of heterogeneity, but requires the consideration of all features identified.

To determine the significance of this observation, consider the null-hypothesis that heterogeneities are randomly distributed with respect to polarization. Taking 10,000 random sets of data equivalent to experiment, but with random heterogeneity locations, the 95% threshold is not reached until a distance two times larger than experiment, see Figure 4d. Further highlighting the difference, the error bars indicate the maximum and minimum 95% distances for the 10,000 datasets at each composition. A result similar to experiment is not found in any of the random data, indicating that $p$ is significantly less than 0.05, safely discounting the null-hypothesis. Taken together, the results presented here unambiguously reveal that chemical and structural heterogeneities are not randomly distributed with respect to polarization, but instead act as the mechanism to disrupt the formation of long-range polarization. Although this role of heterogeneity has been postulated[17,42], its connection to generating low angle domain walls has not been directly observed until now.

## Outlook

The combination of nanoscale features explains the origin for relaxor ferroelectric behavior in PMN-PT that lead to the dramatically improved piezoelectric performance. Thus, to design materials with higher piezoelectric coefficients, balancing order (chemical and/or octahedral distortion/tilt) with disorder is key. In other words, to support relaxor behavior, barriers to polarization rotation need to be distributed throughout the material at a concentration that disrupts long-range (ferroelectric) polarization. For example, this tuning might be achieved by changing the alloy composition, adding dopants, or modifying synthesis conditions. Broadly, engineering a combination of short-range structural and chemical order will be essential for advancing the next generation of Pb-free relaxor-ferroelectric materials.

# References


1. Cohen, R. E. Relaxors go critical. *Nature* **441,** 941–942 (2006).
2. Park, S.-E. & Shrout, T. R. Ultrahigh strain and piezoelectric behavior in relaxor based ferroelectric single crystals. *Journal of Applied Physics* **82,** 1804 (1997).
3. Zhang, S. & Li, F. High performance ferroelectric relaxor-$PbTiO_3$ single crystals: Status and perspective. *Journal of Applied Physics* **111,** 031301 (2012).
4. Zhang, S. *et al.* Advantages and challenges of relaxor-$PbTiO_3$ ferroelectric crystals for electroacoustic transducers - A review. *Prog Mater Sci.* **68,** 1–66 (2015).
5. Burns, G. & Dacol, F. H. Glassy polarization behavior in ferroelectric compounds $Pb(Mg_{1/3}Nb_{2/3})O_3$ and $Pb(Zn_{1/3}Nb_{2/3})O_3$. *Solid State Communications* **48,** 853–856 (1983).
6. Burns, G. & Dacol, F. H. Crystalline ferroelectrics with glassy polarization behavior. *Phys. Rev. B* **28,** 2527–2530 (1983).

7. Yang, L. *et al.* Relaxor ferroelectric behavior from strong physical pinning in a Poly(vinylidene fluoride-co-trifluoroethylene-co-chlorotrifluoroethylene) random terpolymer. *Macromolecules* **47,** 8119–8125 (2014).

8. Takenaka, H., Grinberg, I., Liu, S. & Rappe, A. M. Slush-like polar structures in single-crystal relaxors. *Nature* **546,** 391–395 (2017).

9. Li, F. *et al.* Giant piezoelectricity of Sm-doped $Pb(Mg_{1/3}Nb_{2/3})O_3$-$PbTiO_3$ single crystals. *Science* **364,** 264–268 (2019).

10. Krogstad, M. J. *et al.* The relation of local order to material properties in relaxor ferroelectrics. *Nature Materials* **17,** 718–724 (2018).

11. Singh, A. K., Pandey, D. & Zaharko, O. Powder neutron diffraction study of phase transitions in and a phase diagram of (1-x) $[Pb(Mg_{1/3}Nb_{2/3})O_3]$-$xPbTiO_3$. *Phys. Rev. B* **74,** 024101 (2006).

12. Singh, A. K. & Pandey, D. Evidence for $M_B$ and $M_C$ phases in the morphotropic phase boundary region of (1-x) $[Pb(Mg_{1/3}Nb_{2/3})O_3]$-$xPbTiO_3$: A Rietveld study. *Phys. Rev. B* **67,** 064102 (2003).

13. Thomas, N. W., Ivanov, S. A., Ananta, S., Tellgren, R. & Rundlof, H. New evidence for rhombohedral symmetry in the relaxor ferroelectric $Pb(Mg_{1/3}Nb_{2/3})O_3$. *Journal of the European Ceramic Society* **19,** 2667–2675 (1999).

14. Kim, K. H., Payne, D. A. & Zuo, J. M. Symmetry of piezoelectric (1-x) $Pb(Mg_{1/3}Nb_{2/3})O_3$-$xPbTiO_3$ (x=0.31) single crystal at different length scales in the morphotropic phase boundary region. *Phys. Rev. B* **86,** 184113 (2012).

15. Cowley, R. A., Gvasaliya, S. N., Lushnikov, S. G., Roessli, B. & Rotaru, G. M. Relaxing with relaxors: A review of relaxor ferroelectrics. *Advances in Physics* **60,** 229–327 (2011).

16. Davis, M. Picturing the elephant: Giant piezoelectric activity and the monoclinic phases of relaxor-ferroelectric single crystals. *Journal of Electroceramics* **19,** 25–47 (2007).

17. Randall, C. A. & Bhalla, A. S. Nanostructural-Property Relations in Complex Lead Perovskites. *Japanese Journal of Applied Physics* **29,** 327–333 (1990).

18. Randall, C. A., Bhalla, A. S., Shrout, T. R. & Cross, L. E. Classification and consequences of complex lead perovskite ferroelectrics with regard to B-site cation order. *Journal of Materials Research* **5,** 829–834 (1990).

19. Takesue, N. *et al.* Effects of B-site ordering/disordering in lead scandium niobate. *Journal of Physics: Condensed Matter* **11,** 8301–8312 (1999).

20. Goossens, D. J. Local ordering in lead-based relaxor ferroelectrics. *Acc. Chem. Res.* **46,** 2597–2606 (2013).

21. Cabral, M. J., Zhang, S., Dickey, E. C. & LeBeau, J. M. Gradient chemical order in the relaxor $Pb(Mg_{1/3}Nb_{2/3})O_3$. *Appl. Phys. Lett.* **112,** 082901 (2018).

22. Kopecký, M., Kub, J., Fábry, J. & Hlinka, J. Nanometer-range atomic order directly recovered from resonant diffuse scattering. *Phys. Rev. B* **93,** 054202 (2016).

23. Eremenko, M. *et al.* Local atomic order and hierarchical polar nanoregions in a classical relaxor ferroelectric. *Nat Commun* **10,** 2728 (2019).

24. Rosenfeld, H. D. & Egami, T. Short and intermediate range structural and chemical order in the relaxor ferroelectric lead magnesium niobate. *Ferroelectrics* **164,** 133–141 (1995).

25. Keen, D. A. & Goodwin, A. L. The crystallography of correlated disorder. *Nature* **521,** 303–309 (2015).

26. Xu, G., Wen, J., Stock, C. & Gehring, P. M. Phase instability induced by polar nanoregions in a relaxor ferroelectric system. *Nature Materials* **7,** 562–566 (2008).

27. Findlay, S. D. *et al.* Robust atomic resolution imaging of light elements using scanning transmission electron microscopy. *Appl. Phys. Lett.* **95,** 191913 (2009).

28. Kim, Y. M., Pennycook, S. J. & Borisevich, A. Y. Quantitative comparison of bright field and annular bright field imaging modes for characterization of oxygen octahedral tilts. *Ultramicroscopy* **181,** 1–7 (2017).

29. Lazić, I., Bosch, E. G. & Lazar, S. Phase contrast STEM for thin samples: Integrated differential phase contrast. *Ultramicroscopy* **160,** 265–280 (2016).

30. De Graaf, S., Momand, J., Mitterbauer, C., Lazar, S. & Kooi, B. J. Resolving hydrogen atoms at metal-metal hydride interfaces. *Science Advances* **6,** eaay4312 (2020).

31. Kim, J. *et al.* Epitaxial Strain Control of Relaxor Ferroelectric Phase Evolution. *Adv. Mater.* **31,** 1901060 (2019).

32. Hilton, A. D., Barber, D. J., Randall, C. A. & Shrout, T. R. On short range ordering in the perovskite lead magnesium niobate. *Journal of Materials Science* **25,** 3461–3466 (1990).

33. Kreisel, J. *et al.* High-pressure x-ray scattering of oxides with a nanoscale local structure: Application to $Na_{1/2}Bi_{1/2}TiO_3$. *Phys. Rev. B* **68,** 014113 (2003).

34. Glazer, A. M. The classification of tilted octahedra in perovskites. *Acta Cryst.* **B28,** 3384–3392 (1972).

35. Sang, X., Grimley, E. D., Niu, C., Irving, D. L. & Lebeau, J. M. Direct observation of charge mediated lattice distortions in complex oxide solid solutions. *Appl. Phys. Lett.* **106,** 061913 (2015).

36. Kvyatkovskii, O. E. Oxygen Position in Pb(Mg 1/3 Nb 2/3 )O 3 from ab initio Cluster Calculations. *Ferroelectrics* **299,** 55–57 (2004).

37. Sepliarsky, M. & Cohen, R. E. First-principles based atomistic modeling of phase stability in PMNxPT. *J. Phys.: Condens. Matter* **23,** 435902 (2011).

38. Abramov, Y. A., Tsirelson, V., Zavodnik, V., Ivanov, S. & Brown, I. The chemical bond and atomic displacements in $SrTiO_3$ from X-ray diffraction analysis. *Acta Cryst.* **B51,** 942–951 (1995).

39. Cole, S. S. & Espenschied, H. Lead Titanate: Crystal Structure, Temperature of Formation, and Specific Gravity Data. *J. Phys. Chem* **41,** 445–451 (1937).

40. Shin, Y.-H., Son, J.-Y., Lee, B.-J., Grinberg, I. & Rappe, A. M. Order-disorder character of $PbTiO_3$. *J. Phys.: Condens. Matter* **20,** 015224 (2008).

41. Yoshiasa, A. *et al.* High-temperature single-crystal X-ray diffraction study of tetragonal and cubic perovskite-type $PbTiO_3$ phases. *Acta Cryst. Section B* **72,** 381–388 (2016).

42. Fu, D. *et al.* Relaxor $Pb(Mg_{1/3}Nb_{2/3})O_3$: A Ferroelectric with Multiple Inhomogeneities. *Phys. Rev. Lett.* **103,** 207601 (2009).

**Correspondence and requests for materials** should be addressed to J.M.L.

## Acknowledgements

We gratefully acknowledge support for this work from the National Science Foundation, as part of the Center for Dielectrics and Piezoelectrics under Grant Nos. IIP-1841453 and IIP-1841466. SZ acknowledges support from the Australian Research Council (FT140100698) and the Office of Naval Research Global (N62909-18-12168). PCB was supported by the Department of Defense through the National Defense Science & Engineering Graduate (NDSEG) fellowship program. Computational time and financial support for JNB was provided by AFOSR grant FA9550-17-1-0318. MJC acknowledges support from National Science Foundation as part of the NRT-SEAS under Grant No. DGE-1633587. This work was performed in part at the Analytical Instrumentation Facility (AIF) at North Carolina State University, which is supported by the State of North Carolina and the National Science Foundation (ECCS-1542015). AIF is a member of the North

Carolina Research Triangle Nanotechnology Network (RTNN), a site in the National Nanotechnology Coordinated Infrastructure (NNCI). The NVIDIA Titan Xp GPU used for this research was donated by the NVIDIA Corporation. We acknowledge Matthew Hauwiller for useful suggestions while preparing the manuscript.

## Author Contributions

AK conducted the electron microscopy experiments, data analysis, and image simulations. MJC prepared the PMN samples for electron microscopy and collected STEM data. SZ grew the PMN-xPT single crystals. JNB, PCB, and DLI performed the DFT calculations and the corresponding analysis. JML and ECD designed the electron microscopy experiments and guided the research. All authors co-wrote and edited the manuscript.

# Methods

## Sample Information

$Pb(Mg_{1/3}Nb_{2/3})O_3$-$xPbTiO_3$ (PMN-xPT) single crystals were grown via the high temperature flux method. Samples for electron microscopy were cut from these larger single crystals and oriented along $\langle 1\bar{1}0 \rangle$ and then thinned to electron transparency using mechanical wedge polishing[43] followed by low temperature, low energy Ar ion milling.

## Scanning Transmission Electron Microscopy

STEM imaging was performed with a probe-corrected FEI Titan G2 60-300 kV S/TEM equipped with an X-FEG source at a beam current of 30 pA and probe semi-convergence angle of 19.6 mrad. We used a custom scripting interface to automate the Thermo Fisher Scientific Velox software for simultaneous ADF and iDPC acquisition. ADF images were collected with a semi-collection angle range of 34-205 mrad and iDPC with a collection semi-angle range of 7-28 mrad. For high image accuracy and precision, the revolving STEM (RevSTEM) method was used.[44,45] Each RevSTEM data set consisted of 20 $1024 \times 1024$ pixel frames with a $90^\circ$ rotation between each successive frame. Sample thickness ranged from 6 to 10 nm as determined using position averaged convergent beam electron diffraction[46]. Because, polarization is linearly proportional to the net displacement of cations from anions in an unit cell[47], the projected polarization is calculated from iDPC images as the difference between the cation and anion center of masses. Atom column centers are extracted from drift and scan distortion corrected iDPC images using a custom python based atom column indexing method.[48]

### Density Functional Theory and Image Simulations

Density functional theory (DFT) calculations of PMN were performed to investigate the atomic structures in three dimensions, and to examine charge localization and bond length distributions. These calculations were performed with the PBE exchange correlation functional in VASP 5.3.3, collinear spin polarization, and a plane wave kinetic energy cutoff of 520 eV.[49–52] A single reciprocal space point at $\Gamma$ was used. Projector Augmented Wave pseudopotentials were used with 2, 11, 4, and 6 valence electrons explicitly treated for Mg, Nb, Pb, and O, respectively. Additional details of the calculation are provided in Supplementary Information Section S5.

For STEM image simulations, supercells were constructed using relaxed structures from DFT. A repeating unit was cropped and simulated using a custom python based STEM image simulation software. Simulated ADF and iDPC images were convolved with a Gaussian with full-width at half-maximum of 80 pm to approximately account for the finite effective source size[53].

## Data availability

The image datasets analysed during the current study are available from https://doi.org/10.7910/DVN/F0FHTG. Other data is available from the corresponding author by reasonable request.

## Code availability

Custom Python scripts used to analyse STEM images are available from the corresponding author upon request.

# References


43. Voyles, P. M., Muller, D. A., Grazul, J. L., Citrin, P. H. & Gossmann, H.-J. L. Atomic-scale imaging of individual dopant atoms and clusters in highly n-type bulk Si. *Nature* **416,** 826–829 (2002).

44. Sang, X. & LeBeau, J. M. Revolving scanning transmission electron microscopy: Correcting sample drift distortion without prior knowledge. *Ultramicroscopy* **138,** 28–35 (2014).

45. Dycus, J. H. *et al.* Accurate Nanoscale Crystallography in Real-Space Using Scanning Transmission Electron Microscopy. *Microsc. Microanal.* **21,** 946–952 (2015).

46. LeBeau, J. M., Findlay, S. D., Allen, L. J. & Stemmer, S. Position averaged convergent beam electron diffraction: Theory and applications. English. *Ultramicroscopy* **110,** 118–125 (2010).

47. Tao, H. *et al.* Ultrahigh Performance in Lead-Free Piezoceramics Utilizing a Relaxor Slush Polar State with Multiphase Coexistence. *J. Am. Chem. Soc.* **141,** 13987–13994 (2019).

48. Sang, X., Oni, A. A. & Le Beau, J. M. Atom column indexing: Atomic resolution image analysis through a matrix representation. *Microsc. Microanal.* **20,** 1764–1771 (2014).

49. Kresse, G. & Hafner, J. Ab Initio Molecular Dynamics of Liquid Metals. *Phys. Rev. B* **47,** 558–561 (1993).

50. Kresse, G. & Hafner, J. Ab Initio Molecular-Dynamics Simulation of the Liquid-Metal-Amorphous-Semiconductor Transition in Germanium. *Phys. Rev. B* **49,** 14251–14269 (1994).

51. Kresse, G. & Furthmüller, J. Efficiency of ab-initio total energy calculations for metals and semiconductors using a plane-wave basis set. *Computational Materials Science* **6,** 15–50 (1996).

52. Kresse, G. & Furthmüller, J. Efficient iterative schemes for ab initio total-energy calculations using a plane-wave basis set. *Phys. Rev. B* **54,** 11169–11186 (1996).

53. LeBeau, J. M., Findlay, S. D., Allen, L. J. & Stemmer, S. Quantitative atomic resolution scanning transmission electron microscopy. *Phys. Rev. Lett.* **100,** 206101 (2008).

## Competing interests

The authors declare no competing interests.